

Thioxanthone-based thermally activated delayed fluorescence emitters showing fast reverse intersystem crossing for efficient organic light-emitting diodes with small efficiency roll-off

Yongxia Ren

Kyoto University

Yoshimasa Wada

Kyoto University

Katsuaki Suzuki

Kyoto University

Yu Kusakabe

Kyoto University

Jan Geldsetzer

Kyoto University

Hironori Kaji (✉ kaji@scl.kyoto-u.ac.jp)

Kyoto University

Research Article

Keywords: Thermally activated delayed fluorescence-based organic light-emitting diodes (TADF OLEDs), fast reverse intersystem crossing, Excited states

Posted Date: March 16th, 2021

DOI: <https://doi.org/10.21203/rs.3.rs-289667/v1>

License:   This work is licensed under a Creative Commons Attribution 4.0 International License. [Read Full License](#)

Abstract

Thermally activated delayed fluorescence-based organic light-emitting diodes (TADF OLEDs) usually suffer from severe efficiency roll-off at high brightness which is considered to originate from slow reverse intersystem crossing (RISC) and resulting long-lived triplet excitons. The development of TADF molecules with very fast RISC is an effective approach to overcome this issue. Here, we report two TADF molecules (MCz-TXO, DMCz-TXO) having thioxanthone as an acceptor unit to introduce heavy atom effect. Theoretical calculations predict that both molecules will achieve close energy level matching of the charge-transfer and locally excited triplet states (${}^3\text{CT}$ and ${}^3\text{LE}$, respectively), together with a small energy gap between ${}^3\text{CT}$ and the lowest excited singlet state. The newly designed molecule, MCz-TXO, showed an extremely large rate constant of RISC (k_{RISC}) of $6.4 \times 10^7 \text{ s}^{-1}$, one of the largest k_{RISC} values among all reported pure organic TADF emitters. Moreover, DMCz-TXO showed not only a large k_{RISC} but also a large rate constant of radiative decay both exceeding 10^7 s^{-1} , offering a sub-microsecond-scale delayed lifetime ($\sim 0.8 \mu\text{s}$). These thioxanthone-based emitters exhibited great device performances with suppressed efficiency roll-offs at high luminance when applied to OLEDs.

Introduction

In 2012, Adachi and co-workers reported a thermally activated delayed fluorescence (TADF) organic electroluminescent material, 4CzIPN,¹ which paves the way toward the design and wide applications of the low-cost and highly efficient organic light-emitting diodes (OLEDs). Most of the TADF materials were composed of electron donor (D) and acceptor (A) moieties with a large torsion angle between them, which causes well separated highest occupied molecular orbital (HOMO) and lowest unoccupied molecular orbital (LUMO) distributions on the D and A moieties, respectively.^{2,3} This kind of molecular design leads to a considerably small energy gap (ΔE_{ST}) between the lowest excited singlet and the lowest excited triplet states (S_1 and T_1 , respectively).⁴⁻⁶ Theoretically, TADF materials in OLEDs can utilize all electro-generated triplet excitons for luminescence via a reverse intersystem crossing (RISC) process^{7,8} and realize unity internal quantum efficiencies (IQE).^{1,9-11} This offers a great advantage over the traditional fluorescence materials, whose IQE are at most 25% as only singlet excitons could be converted into light, and over the triplet-triplet annihilation (TTA) emitters showing the highest IQE of 62.5%.¹² Moreover, metal-free and pure organic TADF materials compensate for the drawbacks of phosphorescent emitters, such as limited global resources of noble metals and the expensive material cost, whilst maintaining high IQE.

However, TADF OLEDs usually suffer from efficiency roll-off at high brightness due to the long-lived T_1 excitons, as observed from long-delayed fluorescence with the lifetime ranging from several microseconds to milliseconds.¹³⁻¹⁵ The delayed fluorescence of TADF materials occurs via a RISC ($T_1 \rightarrow S_1$) process followed by a radiative decay ($S_1 \rightarrow$ the ground state (S_0)) pathway. The relatively long-delayed lifetime is closely related to the small rate constant of RISC (k_{RISC}), as reported that RISC process is the rate-limiting process of the TADF.^{16,17} The slow RISC process will cause a substantial build-up of triplet excitons, leading to various types of exciton annihilations and severe efficiency roll-off. However, up to now, there have been only few TADF molecules that show k_{RISC} over 10^7 s^{-1} .¹⁸⁻²¹ According to the Fermi's golden rule, as shown in equation (1),²² k_{RISC} depends on the magnitude of the spin-orbit coupling (SOC) and inversely depends on ΔE_{ST} .

$$k_{\text{RISC}} = A \exp\left(-\frac{\Delta E_{\text{ST}}}{k_{\text{B}}T}\right) \left| \langle S_1 | \hat{H}_{\text{SOC}} | T_1 \rangle \right|^2 \quad (1)$$

where A is a prefactor, $|\langle S_1 | \hat{H}_{\text{SOC}} | T_1 \rangle|$ denotes SOC matrix element values (SOCMEVs) between S_1 and T_1 , k_{B} and T are Boltzmann constant and temperature, respectively. Many reported D-A type TADF molecules possessed charge transfer (CT)-type S_1 and T_1 (^1CT and ^3CT , respectively) with small ΔE_{ST} , but SOC

between ^1CT and ^3CT has been often negligible. Therefore, according to the well-known El-Sayed's rule,²³ fast spin inversion cannot be expected. The inclusion of locally excited triplet state (^3LE) has been proposed in recent years, because larger SOCMEVs can be expected between ^3LE and ^1CT .²⁴⁻³¹ More recently, we have demonstrated that a robust molecular design to realize the close energy level matching of ^1CT , ^3CT , and ^3LE , leading to sufficient SOCMEVs for RISC.^{18,32} The first example molecule (TpAT-tFFO) composing only of H, C, N achieved a very fast RISC rate constant over 10^7 s^{-1} , in spite that no heavy atom effect is expected.¹⁸ As we mentioned in the paper,¹⁸ far larger SOC can be expected by incorporating relatively heavier organic atoms, typically sulfur, into emitter molecules, which can pave the way toward further improvement of k_{RISC} . For example, thioxanthone (TXO) containing sulfur atom can be a promising candidate for achieving very fast RISC and for developing efficient TADF materials owing to the heavy atom effect.³³

In this study, we developed two TXO-based TADF materials, named MCz-TXO and DMCz-TXO (Fig. 1a). Here, the sulfur is introduced in MCz-TXO instead of oxygen in MCz-XT³⁴ (see Supplementary Fig. S3). Therefore, heavy atom effect is expected in MCz-TXO. Theoretical calculations also indicate that MCz-TXO realizes excellent energy level matching of the three states, ^1CT , ^3CT , and ^3LE . These effects resulted in considerably large experimental k_{RISC} of $6.4 \times 10^7 \text{ s}^{-1}$ for MCz-TXO, thirty times larger than that of MCz-XT. We also designed D-A-D type TADF molecule, DMCz-TXO, to obtain larger rate constant of radiative decay from S_1 (k_{r}). Experimentally, DMCz-TXO exhibited $k_{\text{r}} = 1.2 \times 10^7 \text{ s}^{-1}$ and $k_{\text{RISC}} = 3.4 \times 10^7 \text{ s}^{-1}$, the first TADF molecule realizing both k_{r} and k_{RISC} exceeding 10^7 s^{-1} to the best of our knowledge. Due to the very large k_{r} and k_{RISC} , DMCz-TXO showed a very short lifetime ($\sim 0.8 \mu\text{s}$) of the delayed fluorescence. The DMCz-TXO-based OLED exhibited maximum external quantum efficiency (EQE_{MAX}) of $> 20\%$ and maximum luminance of $> 20,000 \text{ cd m}^{-2}$ with suppressed efficiency roll-off (EQE of 20.5% and 19.1% with efficiency roll-off of only 0.2% and 7.0% at 100 cd m^{-2} and $1,000 \text{ cd m}^{-2}$, respectively) without any outcoupling treatment.

Results And Discussion

Theoretical calculations. The two TADF molecules were designed using TXO moiety as an acceptor coupled with one or two 1,3,6,8-tetramethylcarbazole (MCz) as electron-donating units, namely, MCz-TXO and DMCz-TXO (Fig. 1a), respectively. Here, TXO fragment is likely to realize stronger SOC due to the heavy atom effect introduced by sulfur, thus endowing the molecules with larger k_{RISC} and higher TADF efficiency. Considering that k_{r} is also important to control the exciton lifetimes,²² the D-A-D structure is adopted to expect higher k_{r} .^{16,35} To verify our design strategy, density functional theory (DFT) and time-dependent DFT with Tamm-Dancoff approximation (TDA-DFT) calculations were carried out by Amsterdam Density Functional program package (ADF2019.302).³⁶ We used PBE0 functional with triple zeta basis set for geometry optimization of S_0 . The

highest occupied natural transition orbitals (HONTOs) and the lowest unoccupied natural transition orbitals (LUNTOs) were visualized to understand the nature of multiple excited states, together with the corresponding energy levels of the states (Fig. 1, Supplementary Fig. S4 and Supplementary Table S1). SOCMEVs between S_1 and T_n (where $n = 1-5$) were also calculated as shown in Table 1.

MCz-TXO and DMCz-TXO have very small ΔE_{ST} of 0.03 eV and 0.01 eV, respectively, due to the well-separated HOMO and LUMO as shown in Fig. 1a. Both molecules possess CT-type S_1 and T_1 . Figure 1b shows HONTO and LUNTO of MCz-TXO. T_2 has LE character and thus large SOCMEV between T_2 (3LE) and S_1 (1CT) is expected. In addition, T_2 is close to S_1 in energy with the downhill energy gap from T_2 to S_1 ($\Delta E_{S_1-T_2}$) of 0.20 eV. As shown in Table 1, a considerably large SOCMEV of 4.68 cm^{-1} is found between the T_2 (3LE) and S_1 (1CT) in MCz-TXO. For DMCz-TXO (Fig. 1c), both T_1 and T_2 are CT-type but T_3 is LE with a small downhill energy gap between T_3 and S_1 , $\Delta E_{S_1-T_3}$, of 0.18 eV. A similarly large SOCMEV of 6.01 cm^{-1} is found between T_3 (3LE) and S_1 (1CT) in DMCz-TXO.

To investigate the heavy atom effect introduced by the sulfur atom in TXO, we also conducted calculations on a reported molecule, MCz-XT (see Supplementary Fig. S3), for comparison. MCz-XT has the same chemical structure as MCz-TXO except that the oxygen atom is replaced with sulfur.³⁴ Therefore, the heavy atom effect of sulfur can be investigated directly by the comparison. As shown in Supplementary Fig. S3, similar to MCz-TXO, MCz-XT exhibited well separated HOMO and LUMO with a similarly large torsion angle of 81° . For MCz-XT (see Supplementary Table S1), S_1 and T_1 are CT-type. T_2 is hybridized local and charge-transfer (HLCT) type, but is a CT-dominant character. In contrast, T_3 is LE-dominant HLCT type, showing the largest SOCMEV in MCz-XT of 1.04 cm^{-1} for T_3 (3LE) \rightarrow S_1 (1CT) transition (Table 1). For MCz-TXO, HONTO and LUNTO of S_1 and T_1 are very similar to those of MCz-XT, but HONTO of T_2 is significantly different. T_2 of MCz-TXO is LE-type and the distribution on sulfur is very large (see Supplementary Table S1), resulting in the very large SOCMEV of 4.68 cm^{-1} for T_2 (3LE) \rightarrow S_1 (1CT) transition in MCz-TXO, far larger than the largest SOCMEV in MCz-XT, 1.04 cm^{-1} . Besides, the energy difference between 3LE and 1CT of MCz-TXO, 0.20 eV, is much smaller than that of MCz-XT, 0.59 eV. Although both the transitions are downhill in energy, the energy mismatch for MCz-XT makes the internal conversion from T_1 (3CT) to T_3 (3LE) ineffective (the energy difference: 0.62 eV), resulting in the difficulty of the participation of T_3 (3LE) in the RISC process. Therefore, only the direct $^3CT \rightarrow ^1CT$ transition with SOCMEV of 0.13 cm^{-1} and energy difference of 0.03 eV is expected for MCz-XT (the experimental k_{RISC} was $\sim 2 \times 10^6 \text{ s}^{-1}$). On the basis of the discussion, we can expect a far larger k_{RISC} value for MCz-TXO, because the LE-dominant T_2 can be incorporated into the RISC process due to the relatively small energy difference (0.20 eV) and the large SOCMEV of 4.68 cm^{-1} between T_2 (3LE) and S_1 (1CT). Similarly, DMCz-TXO (SOCMEV of 6.01 cm^{-1} and energy difference of -0.18 eV for $T_3 \rightarrow S_1$ transition) is also expected to show large k_{RISC} .

Table 1. The calculated SOCMEVs together with the energy difference between S_1 and the triplet states (T_n) for MCz-XT, MCz-TXO, and DMCz-TXO. ^aThe nature of the state is shown in parentheses.

| Molecule | SOCMEV | | | | | |
|----------|------------------------|------------------------------------|-------------------------------------|--------------------------------------|-------------------------------------|-------------------------------------|
| | / $\Delta E_{S_1-T_n}$ | | | | | |
| MCz-XT | | T ₁ (CT) ^a | T ₂ (CT) | T ₃ ($\pi\pi^*_{A+CT}$) | T ₄ ($n\pi^*_{A}$) | T ₅ ($\pi\pi^*_{D}$) |
| | S ₁ (CT) | 0.13 cm ⁻¹ / 0.03 eV | 0.30 cm ⁻¹ / -0.44 eV | 1.04 cm ⁻¹ / -0.59 eV | 0.98 cm ⁻¹ / -0.60 eV | 0.33 cm ⁻¹ / -0.66 eV |
| MCz-TXO | | T ₁ (CT) | T ₂ ($\pi\pi^*_{A}$) | T ₃ (CT) | T ₄ ($n\pi^*_{A}$) | T ₅ ($\pi\pi^*_{D}$) |
| | S ₁ (CT) | 0.30 cm ⁻¹ / 0.03 eV | 4.68 cm ⁻¹ / -0.20 eV | 0.95 cm ⁻¹ / -0.48 eV | 1.19 cm ⁻¹ / -0.56 eV | 0.23 cm ⁻¹ / -0.67 eV |
| DMCz-TXO | | T ₁ (CT) | T ₂ (CT) | T ₃ ($\pi\pi^*_{A}$) | T ₄ (CT) | T ₅ (CT) |
| | S ₁ (CT) | 0.01 cm ⁻¹ / 0.01 eV | 0.47 cm ⁻¹ / -0.01 eV | 6.01 cm ⁻¹ / -0.18 eV | 0.35 cm ⁻¹ / -0.40 eV | 0.99 cm ⁻¹ / -0.41 eV |

Photophysical properties. Photophysical measurements of MCz-TXO and DMCz-TXO in 10^{-4} M oxygen-free toluene solution were conducted to evaluate their TADF efficiencies. The ultraviolet-visible (UV-vis) absorption spectra, photoluminescence (PL) spectra of MCz-TXO and DMCz-TXO were shown in Fig. 2. The absorption band in the range of 300 to 350 nm and the range of 350 to 380 nm in the UV-vis spectra correspond to the absorption of MCz and TXO, respectively.^{37,38} The absorption around 400–450 nm can be attributed to intramolecular CT (ICT) absorption from MCz to TXO and the intensity of ICT absorption of DMCz-TXO is much larger than that of MCz-TXO, although it overlapped partly with the absorption of the TXO at a shorter wavelength. The emission peak maximum wavelength (λ_{MAX}) was 480 nm for MCz-TXO and 491 nm for DMCz-TXO. The PL quantum yield (PLQY or Φ_{PL}) and transient PL measurements were also conducted for two compounds in 10^{-4} M oxygen-free toluene solution at ambient temperature. The transient PL data, in Fig. 2b, exhibited double exponential decay curves with $\tau_{PF}/\tau_{DF} = 0.8$ ns/1.2 μ s for MCz-TXO and 1.8 ns/0.8 μ s for DMCz-TXO, respectively. Here, τ_{PF} and τ_{DF} are the lifetimes of prompt and delayed fluorescences, respectively. To understand the origin of the very fast delayed fluorescence, we performed a detailed analysis of related rate constants for the MCz-TXO and DMCz-TXO according to the reported equation, which is suitable for the TADF molecules showing large k_{RISC} .¹⁸ The experimental and the analyzed data are summarized in Table 2. For comparison, the reported photophysical performance of 5 vol% MCz-XT:PPF film was also cited in Table 2. As we expected, both MCz-TXO and DMCz-TXO showed very large k_{RISC} , exceeding 10^7 s⁻¹. When compared to the k_{RISC} value of MCz-XT ($\sim 2 \times 10^6$ s⁻¹), MCz-TXO achieved thirty times larger k_{RISC} of 6.4×10^7 s⁻¹, confirming the heavy atom effect introduced by sulfur. We assume that our strategy can be widely adopted in various TADF molecular designs for further RISC enhancement. DMCz-TXO also showed a large k_{RISC} of 3.4×10^7 s⁻¹ and large k_r of 1.2×10^7 s⁻¹, providing a sub-microsecond-scale τ_{DF} of 0.8 μ s. To our best knowledge, DMCz-TXO is the first organic molecule showing both k_r and k_{RISC} exceeding 10^7 s⁻¹, simultaneously.

The photophysical performance of the doped films were also examined. Here, MCz-TXO and DMCz-TXO were doped in 9-(4-tertbutylphenyl)-3,6-bis(triphenylsilyl)-9H-carbazole (CzSi) and 3,3'-di(9H-carbazol-9-yl)-1,1'-biphenyl (mCBP), respectively. As shown in Supplementary Table S2, the MCz-TXO:CzSi film with an optimal concentration of 5 vol% provided Φ_{PL} of 64.7% and λ_{MAX} of 475 nm with Commission Internationale de l'Eclairage (CIE) coordinates of (0.16, 0.22). The transient PL curve of 5 vol% MCz-TXO:CzSi film showed multi-

delayed fluorescence and the detailed analysis was not carried out. For DMCz-TXO-doped films (see Supplementary Table S3), Φ_{PL} of 100% was obtained for 5 vol% DMCz-TXO:mCBP film with λ_{MAX} of 492 nm and CIE of (0.21, 0.40). The transient PL decay curves (Fig. 2c) showed a very fast prompt fluorescence with nanosecond-scale τ_{PF} of 3.0 ns and a very fast delayed fluorescence with a sub-microsecond-scale τ_{DF} of 0.8 μ s. The detailed analysis provides rate constants of $k_r = 1.5 \times 10^7 \text{ s}^{-1}$, $k_{RISC} = 2.9 \times 10^7 \text{ s}^{-1}$, and $k_{ISC} = 3.0 \times 10^8 \text{ s}^{-1}$ with completely suppressed non-radiative decay from S_1 (PLQY of 100%) (see Supplementary Table S3). From an Arrhenius plot of k_{RISC} for the 5 vol% DMCz-TXO:mCBP film (Fig. 2d), the activation energy was estimated to be 53 meV. Moreover, DMCz-TXO still possessed a high k_{RISC} of $8.5 \times 10^6 \text{ s}^{-1}$ even at low temperature of 200 K (see Supplementary Table S4), which is higher than that of most of TADF materials at 300 K, indicating that the inclusion of 3LE , together with the heavy atom effect by sulfur, enhance RISC process effectively.

Table 2

The photophysical performance of MCz-TXO and DMCz-TXO in 10^{-4} M oxygen-free toluene solution, and 5 vol% DMCz-TXO:mCBP film. The values for 5 vol% MCz-TXO:PPF film are also listed for comparison. ^aThe related data were obtained in 10^{-4} M oxygen-free toluene solution. ^bThe total (Φ_{PL}), prompt (Φ_{PF}), and delayed (Φ_{DF}) photoluminescence efficiency yield. ^cThe rate constant of reverse intersystem crossing (k_{RISC}), intersystem crossing (k_{ISC}), radiative decay (k_r), and nonradiative decay (k_{nr}). ^dPLQY was measured under excitation wavelength at 405 nm for DMCz-TXO and 365 nm for MCz-TXO, respectively. ^ePhotophysical properties of MCz-TXO in a PPF host matrix at doping concentrations of 5 wt%, cited from ref. 34. ^fThe rate constants were calculated using the reported method in ref. 18. ^gThe data were for the 5 vol% DMCz-TXO:mCBP film. ^hPLQY was determined under nitrogen atmosphere at the excitation wavelength of 380 nm.

| Emitter | Environment | λ_{MAX} (nm) | τ_{PF} (ns) | τ_{DF} (μ s) | Φ_{PL}^b (%) | Φ_{PF}^b (%) | Φ_{DF}^b (%) | k_{RISC}^c (10^7 s^{-1}) | k_{ISC}^c (10^8 s^{-1}) | k_r^c (10^7 s^{-1}) | k_{nr}^c (10^6 s^{-1}) |
|-----------------------|------------------|-------------------------|---------------------|---------------------------|----------------------|----------------------|----------------------|---|--|--|---|
| DMCz-TXO ^a | Toluene Solution | 491 | 1.8 | 0.8 | 60.2 ^d | 2.3 | 57.9 | 3.4 | 5.1 | 1.2 | 8.1 |
| MCz-TXO ^a | Toluene Solution | 480 | 0.8 | 1.2 | 40.3 ^d | 0.6 | 39.7 | 6.4 | 11.7 | 0.7 | 9.9 |
| MCz-TXO ^e | Doped in PPF | / | 33.3 | 1.2 | 98.0 | 41.4 | 56.6 | \sim 0.2 ^f | \sim 0.2 ^f | 1.2 ^f | \sim 0.2 ^f |
| DMCz-TXO ^g | Doped in mCBP | 492 | 3.0 | 0.8 | 100.0 ^h | 4.7 | 95.3 | 2.9 | 3.0 | 1.5 | 0.0 |

OLED properties. To evaluate the potential of our designed molecules as TADF emitters, the MCz-TXO based device is prepared using the following structure: indium-tin-oxide (ITO) (50 nm)/4,4'-cyclohexylidenebis[*N,N*-bis(4-methylphenyl) benzenamine] (TAPC) (60 nm)/1,3-bis(9,9-dimethylacridin-10(9H)-yl)benzene (mAP) (10 nm)/5 vol% MCz-TXO:CzSi (20 nm)/2,8-bis(diphenylphosphoryl)dibenzo[*b,d*]furan (PPF) (10 nm)/1,3-bis[3,5-di(pyridin-3-yl)phenyl]benzene (BmPyPhB)³⁹ (30 nm)/lithium quinolin-8-olate (Liq) (1 nm)/Al (80 nm) (Supplementary Fig. S7). The structure of DMCz-TXO based device (as shown in Fig. 3a) is ITO

Table 3

The summary of OLED performances using MCz-TXO, DMCz-TXO, and the reported TXO-based TADF materials as emitters. ^aat 100 cd m⁻². ^bEQE_{MAX} means maximum EQE value. EQE_Y means EQE value at Y cd m⁻². ^cN.A. means that data was not provided in the related reference. ^d/ means no data available.

| Emitter | CIE(x, y) ^a | EQE _{MAX} ^b (%) | EQE ₁₀₀ ^b (%) | EQE _{1,000} ^b (%) | EQE _{10,000} ^b (%) | EQE _{20,000} ^b (%) | L _{MAX} ^b (cd m ⁻²) | Ref. |
|---------------------------|------------------------|--|--|--|---|---|--|-----------|
| 5 vol% DMCz-TXO:mCBP | (0.20, 0.45) | 20.5 | 20.5 | 19.1 | 14.0 | 9.8 | 23,180 | This work |
| 5 vol% MCz-TXO:CzSi | (0.15, 0.21) | 17.4 | 14.3 | 7.8 | / ^d | / | 2,097 | This work |
| 10 wt% CzTXO:DPEPO | (0.16, 0.20) | 11.2 | N.A. ^c | / | / | / | 183 | 40 |
| 10 wt% DCzTXO:DPEPO | (0.18, 0.37) | 11.5 | N.A. | / | / ^c | / | 627 | 40 |
| 10 wt% 1,6-2TPA-TX:CBP | (0.41, 0.55) | 2.2 | 0.8 | 0.4 | / | / | < 5,000 | 41 |
| 3 wt% 3,6-2TPA-TX:CBP | (0.14, 0.28) | 23.7 | 4.4 | 3.2 | / | / | < 10,000 | 41 |

(50 nm)/TAPC (60 nm)/mAP (10 nm)/5 vol% DMCz-TXO:mCBP (30 nm)/PPF (10 nm)/BmPyPhB (35 nm)/Liq (1 nm)/Al (80 nm). TAPC and BmPyPhB were used as hole and electron transport layers, respectively. The mAP and PPF possessing high T₁ energy (3.0 eV and 3.1 eV, respectively) were inserted in both sides of the emitting layers to confine excitons. The electroluminescent performances were listed in Fig. 3 and Table 3.

The device using 5 vol% MCz-TXO:CzSi as an emitter layer exhibited sky-blue emission with the peak maximum wavelength at 469 nm and CIE of (0.15, 0.21) at 100 cd m⁻². The device achieved EQE_{MAX} of 17.4% owing to a relatively high ϕ_{PL} of 64.7%. DMCz-TXO based device with an optimal doping concentration of 5 vol% achieves EQE_{MAX} of 20.5% and high luminance (> 20,000 cd m⁻²) without any outcoupling treatment. Besides, the device showed suppressed efficiency roll-off; the EQEs were 20.5% and 19.1% (the efficiency roll-offs were only 0.2% and 7.0%) at the luminance of 100 and 1,000 cd m⁻², respectively. The EQEs at 10,000 and 20,000 cd m⁻² were still high, namely 14.0% and 9.8% respectively. The high k_{RISC} (> 10⁷ s⁻¹) and k_f (> 10⁷ s⁻¹) of DMCz-TXO can prevent the accumulation of triplet excitons, thus suppressing singlet-triplet annihilation and triplet-triplet annihilation process, giving rise to reduced efficiency roll-off.

Previously, there are two reports about the TXO-based TADF molecules and the related OLED performances were also summarized in Table 3.⁴⁰ Among these OLEDs using TXO as an acceptor of TADF emitters, MCz-TXO-based OLED showed blue emission with slightly reduced efficiency roll-off. Besides, the DMCz-TXO-based OLED also exhibited greatly improved roll-off suppression, clearly exemplifying the great advantage of simultaneous realization of very fast RISC and radiative decay with the rate constants both over 10^7 s^{-1} .

In conclusion, a newly-designed molecule, MCz-TXO, showed (1) good energy level matching of the three states, ^1CT , ^3CT , ^3LE ; (2) heavy atom effect introduced by sulfur, thus possessing considerably large k_{RISC} of $6.4 \times 10^7 \text{ s}^{-1}$, one of the largest k_{RISC} among all reported pure organic TADF emitters. The value is thirty times larger than that of the molecule which has the same chemical structure as MCz-TXO except that the oxygen atom is replaced with sulfur, confirming the effectiveness of our design concept. We believe that this concept, namely, good matching of ^1CT , ^3CT , and ^3LE , together with the incorporation of heavier organic atoms (such as S, Se), can be applied to various TADF materials, for further improvement of k_{RISC} and thus the enhancement of TADF efficiency. Moreover, a higher radiative decay rate constant is also of vital importance to shorten the delayed lifetime and realize a small efficiency roll-off for OLEDs. As demonstrated in this study, DMCz-TXO, possessed k_{RISC} of $3.4 \times 10^7 \text{ s}^{-1}$ and k_{r} of $1.2 \times 10^7 \text{ s}^{-1}$, offering a sub-microsecond-scale delayed lifetime. The DMCz-TXO-based OLED exhibited great device performance with suppressed efficiency roll-off when applied to OLEDs. In the future, these kinds of TADF molecules showing very fast triplet-to-singlet conversion can also be promisingly used as are TADF-assistant dopants in hyperfluorescent OLEDs for realizing various emission color or achieving better performance.^{12,18,42,43}

Methods

Sample preparation and material characterization. The detailed synthesis procedure is listed in the Supplementary Information. Samples for all the experiments were further purified using the train sublimation method. ^1H and ^{13}C NMR spectra of MCz-TXO and DMCz-TXO were collected using a Bruker Avance-III (800 MHz for ^1H , 201 MHz for ^{13}C) and summarized in the Supplementary Information. The temperature corresponding to 5% weight loss (decomposition temperature, T_{d}) of the thermogravimetric analysis (TGA) curves at atmospheric pressure and the points corresponding to 50% (sublimation temperature, T_{sub}) weight loss of the TGA curves at 100 Pa are indicated in Supplementary Fig. S1. The glass transition temperatures were determined from the onset of the differential scanning calorimetry (DSC) curves (see Supplementary Fig. S2).

Characterization for photophysical measurements. PLQY (or Φ_{PL}) was measured with an absolute PLQY spectrometer (C9920-02, Hamamatsu Photonics, Japan). MCz-TXO or DMCz-TXO in oxygen-free toluene solutions at a concentration of $1.0 \times 10^{-4} \text{ M}$ were prepared in the glove box where the concentration of oxygen and water are less than 0.1 ppm. The PLQY values in 10^{-4} M oxygen-free toluene solution were collected under excitation wavelengths at 405 nm for DMCz-TXO and at 365 nm for MCz-TXO. Neat or doped films were fabricated using a vacuum-deposited method at $\sim 10^{-5} \text{ Pa}$ on clean quartz glass substrates. The PLQYs of films were measured under N_2 atmosphere. UV-vis absorption spectra and PL spectra were collected using a UV-vis spectrophotometer (UV-2600, SHIMAZU, Japan) and a spectrofluorometer (FluoroMax Plus, HORIBA, Japan), respectively. The temperature-dependent transient PL decay measurements were conducted with a fluorescence

lifetime measurement system (Quantaaurus-Tau C11367-01, Hamamatsu Photonics, Japan) equipped with a cryostat (Oxford Instruments, Optistat DN2, UK).

Device fabrication and characterization. The ITO substrates were precleaned carefully before use. Multi-layers OLEDs with active areas of 4 mm² were fabricated under vacuum at a pressure of $\sim 10^{-4}$ Pa with a deposition apparatus (SE-4260, ALS Technology, Japan). OLED characteristics were measured with a source meter (2400, Keithley, Japan) and an absolute EQE measurement system (C9920-12, Hamamatsu Photonics, Japan). The applied voltage during device performance tests was increased with an increment of 200 meV.

Declarations

Competing interests

The authors declare no competing financial interests.

Acknowledgements

We thank Kyulux, Inc. and JSPS KAKENHI Grant Numbers JP20H05840 (Grant-in-Aid for Transformative Research Areas, “Dynamic Exciton”), JP 17H01231 for their financial supports. Computation time was provided by the Super Computer System, Institute for Chemical Research, Kyoto University. NMR measurements were supported by the international Joint Usage/Research Centre (iJURC) at the Institute for Chemical Research, Kyoto University, Japan.

Author contributions

H.K. conceived and supervised the project. K.S. designed the molecular structures based on theoretical calculations. J.G. performed the syntheses. Y.R. and Y.W. carried out detailed theoretical calculations. Y.R. performed photophysical measurements, device fabrications, device performance measurements, data analysis, and figure generation. Y.W. supported Y.R., designed the device structure, and did the data analysis. Y.K. supported photophysical measurements, device performance measurements, and data analysis. All authors contributed to the writing of this manuscript and have approved the final version of the manuscript.

Additional Information

Supplementary information accompanies this paper at XXX

References

1. Uoyama, H., Goushi, K., Shizu, K., Nomura, H. & Adachi, C. Highly efficient organic light-emitting diodes from delayed fluorescence. *Nature*. **492**, 234–238 (2012).
2. Wong, M. Y. & Zysman-Colman, E. Purely Organic Thermally Activated Delayed Fluorescence Materials for Organic Light-Emitting Diodes. *Adv. Mater.* **29**, 1605444 (2017).
3. Liu, M. *et al.* Introduction of Twisted Backbone: A New Strategy to Achieve Efficient Blue Fluorescence Emitter with Delayed Emission. *Adv. Opt. Mater.* **5**, 1700334 (2017).

4. Cai, X. Y., Gao, B., Li, X. L., Gao, Y. & Su, S. J. Singlet-Triplet Splitting Energy Management via Acceptor Substitution: Complanation Molecular Design for Deep-Blue Thermally Activated Delayed Fluorescence Emitters and Organic Light-Emitting Diodes Application. *Adv. Funct. Mater.* **26**, 8042–8052 (2016).
5. Miwa, T. *et al.* Blue organic light-emitting diodes realizing external quantum efficiency over 25% using thermally activated delayed fluorescence emitters. *Sci. Rep.* **7**, 284 (2017).
6. Zhang, Z. *et al.* Efficient Sky-Blue Organic Light-Emitting Diodes Using a Highly Horizontally Oriented Thermally Activated Delayed Fluorescence Emitter. *Adv. Opt. Mater.* **8**, 2001354 (2020).
7. Kato, Y. *et al.* A sky blue thermally activated delayed fluorescence emitter to achieve efficient white light emission through in situ metal complex formation. *J. Mater. Chem. C.* **7**, 3146–3149 (2019).
8. Ohsawa, T. *et al.* A Series of Imidazo[1,2-f]phenanthridine-Based Sky-Blue TADF Emitters Realizing EQE of over 20%. *Adv. Opt. Mater.* **7**, 1801282 (2019).
9. Lin, T. A. *et al.* Sky-Blue Organic Light Emitting Diode with 37% External Quantum Efficiency Using Thermally Activated Delayed Fluorescence from Spiroacridine-Triazine Hybrid. *Adv. Mater.* **28**, 6976–6983 (2016).
10. Kaji, H. *et al.* Purely organic electroluminescent material realizing 100% conversion from electricity to light. *Nat. Commun.* **6**, 8476 (2015).
11. Hundemer, F. *et al.* Tris(triazolo)triazine-based emitters for solution-processed blue thermally activated delayed fluorescence organic light-emitting diodes. *Mater. Adv.* **1**, 2862–2871 (2020).
12. Nakanotani, H. *et al.* High-efficiency organic light-emitting diodes with fluorescent emitters. *Nat. Commun.* **5**, 4016 (2014).
13. Inoue, M. *et al.* Effect of reverse intersystem crossing rate to suppress efficiency roll-off in organic light-emitting diodes with thermally activated delayed fluorescence emitters. *Chem. Phys. Lett.* **644**, 62–67 (2016).
14. Yang, Z. Y. *et al.* Recent advances in organic thermally activated delayed fluorescence materials. *Chem. Soc. Rev.* **46**, 915–1016 (2017).
15. Wang, D., Cheng, C., Tsuboi, T. & Zhang, Q. S. Degradation Mechanisms in Blue Organic Light-Emitting Diodes. *CCS Chem.* **2**, 1278–1296 (2020).
16. Cai, X. Y. *et al.* "Rate-limited effect" of reverse intersystem crossing process: the key for tuning thermally activated delayed fluorescence lifetime and efficiency roll-off of organic light emitting diodes. *Chem. Sci.* **7**, 4264–4275 (2016).
17. Krotkus, S. *et al.* Fast Delayed Emission in New Pyridazine-Based Compounds. *Front. Chem.* **8**, 572862 (2020).
18. Wada, Y., Nakagawa, H., Matsumoto, S., Wakisaka, Y. & Kaji, H. Organic light emitters exhibiting very fast reverse intersystem crossing. *Nat. Photonics.* **14**, 643–649 (2020).
19. Cui, L. S. *et al.* Fast spin-flip enables efficient and stable organic electroluminescence from charge-transfer states. *Nat. Photonics.* **14**, 636–642 (2020).
20. Mahmoudi, M. *et al.* Exciplex-forming systems with extremely high RISC rates exceeding 10^7 s⁻¹ for oxygen probing and white hybrid OLEDs. *J. Mater. Res. Technol.* **10**, 711–721 (2021).

21. Ricardo, J. V. *et al.* New Direct Approach for Determining the Reverse Intersystem Crossing Rate in Organic Thermally Activated Delayed Fluorescent (TADF) Emitters. *J. Am. Chem. Soc.* **142**, 8074–8079 (2020).
22. Kim, J. U. *et al.* Nanosecond-time-scale delayed fluorescence molecule for deep-blue OLEDs with small efficiency rolloff. *Nat. Commun.* **11**, 1765 (2020).
23. El-Sayed, M. A. Spin-Orbit Coupling and the Radiationless Processes in Nitrogen Heterocyclics. *J. Chem. Phys.* **38**, 2834–2838 (1963).
24. Etherington, M. K., Gibson, J., Higginbotham, H. F., Penfold, T. J. & Monkman, A. P. Revealing the spin-vibronic coupling mechanism of thermally activated delayed fluorescence. *Nat. Commun.* **7**, 13680 (2016).
25. Samanta, P. K., Kim, D., Coropceanu, V. & Bredas, J. L. Up-Conversion Intersystem Crossing Rates in Organic Emitters for Thermally Activated Delayed Fluorescence: Impact of the Nature of Singlet vs Triplet Excited States. *J. Am. Chem. Soc.* **139**, 4042–4051 (2017).
26. Mewes, J. M. Modeling TADF in organic emitters requires a careful consideration of the environment and going beyond the Franck-Condon approximation. *Phys. Chem. Chem. Phys.* **20**, 12454–12469 (2018).
27. Gibson, J., Monkman, A. P. & Penfold, T. J. The Importance of Vibronic Coupling for Efficient Reverse Intersystem Crossing in Thermally Activated Delayed Fluorescence Molecules. *Chemphyschem.* **17**, 2956–2961 (2016).
28. Marian, C. M. Mechanism of the Triplet-to-Singlet Upconversion in the Assistant Dopant ACRXTN. *J. Phys. Chem. C.* **120**, 3715–3721 (2016).
29. Dias, F. B. *et al.* The Role of Local Triplet Excited States and D-A Relative Orientation in Thermally Activated Delayed Fluorescence: Photophysics and Devices. *Adv. Sci.* **3**, 1600080 (2016).
30. Lyskov, I. & Marian, C. M. Climbing up the Ladder: Intermediate Triplet States Promote the Reverse Intersystem Crossing in the Efficient TADF Emitter ACRSA. *J. Phys. Chem. C.* **121**, 21145–21153 (2017).
31. Hosokai, T. *et al.* Evidence and mechanism of efficient thermally activated delayed fluorescence promoted by delocalized excited states. *Sci. Adv.* **3**, e1603282 (2017).
32. Kusakabe, Y., Wada, Y., Nakagawa, H., Shizu, K. & Kaji, H. Conformation Control of Iminodibenzyl-Based Thermally Activated Delayed Fluorescence Material by Tilted Face-to-Face Alignment With Optimal Distance (tFFO) Design. *Front. Chem.* **8**, 530 (2020).
33. Xiang, Y. P. *et al.* Halogen-induced internal heavy-atom effect shortening the emissive lifetime and improving the fluorescence efficiency of thermally activated delayed fluorescence emitters. *J. Mater. Chem. C.* **5**, 12204–12210 (2017).
34. Lee, J., Aizawa, N., Numata, M., Adachi, C. & Yasuda, T. Versatile Molecular Functionalization for Inhibiting Concentration Quenching of Thermally Activated Delayed Fluorescence. *Adv. Mater.* **29**, 1604856 (2017).
35. Gao, F. F. *et al.* High-efficiency blue thermally activated delayed fluorescence from donor-acceptor-donor systems via the through-space conjugation effect. *Chem. Sci.* **10**, 5556–5567 (2019).
36. te Velde, G. *et al.* Chemistry with ADF. *J. Comput. Chem.* **22**, 931–967 (2001).
37. Li, H. H. *et al.* Direct silicon–nitrogen bonded host materials with enhanced σ - π conjugation for blue phosphorescent organic light-emitting diodes. *J. Mater. Chem. C.* **4**, 10047–10052 (2016).
38. Chi, T. *et al.* Tailored thioxanthone-based photoinitiators for two-photon-controllable polymerization and nanolithographic printing. *J. Polym. Sci., Part B: Polym. Phys.* **57**, 1462–1475 (2019).

39. Sasabe, H. *et al.* Wide-Energy-Gap Electron-Transport Materials Containing 3,5-Dipyridylphenyl Moieties for an Ultra High Efficiency Blue Organic Light-Emitting Device. *Chem. Mater.* **20**, 5951–5953 (2008).
40. Wang, Z. H. *et al.* Structure-Performance Investigation of Thioxanthone Derivatives for Developing Color Tunable Highly Efficient Thermally Activated Delayed Fluorescence Emitters. *ACS Appl. Mater. Interfaces.* **8**, 8627–8636 (2016).
41. Li, Y. C. *et al.* Design Strategy of Blue and Yellow Thermally Activated Delayed Fluorescence Emitters and Their All-Fluorescence White OLEDs with External Quantum Efficiency beyond 20%. *Adv. Funct. Mater.* **26**, 6904–6912 (2016).
42. Kim, J. H., Lee, K. H. & Lee, J. Y. Design of thermally activated delayed fluorescent sensitizers for high efficiency over 20% and long lifetime in yellow fluorescent organic light-emitting diodes. *J. Mater. Chem. C.* **8**, 5265–5272 (2020).
43. Zhang, D. *et al.* Efficient and Stable Deep-Blue Fluorescent Organic Light-Emitting Diodes Employing a Sensitizer with Fast Triplet Upconversion. *Adv. Mater.* **32**, 1908355 (2020).

Figures

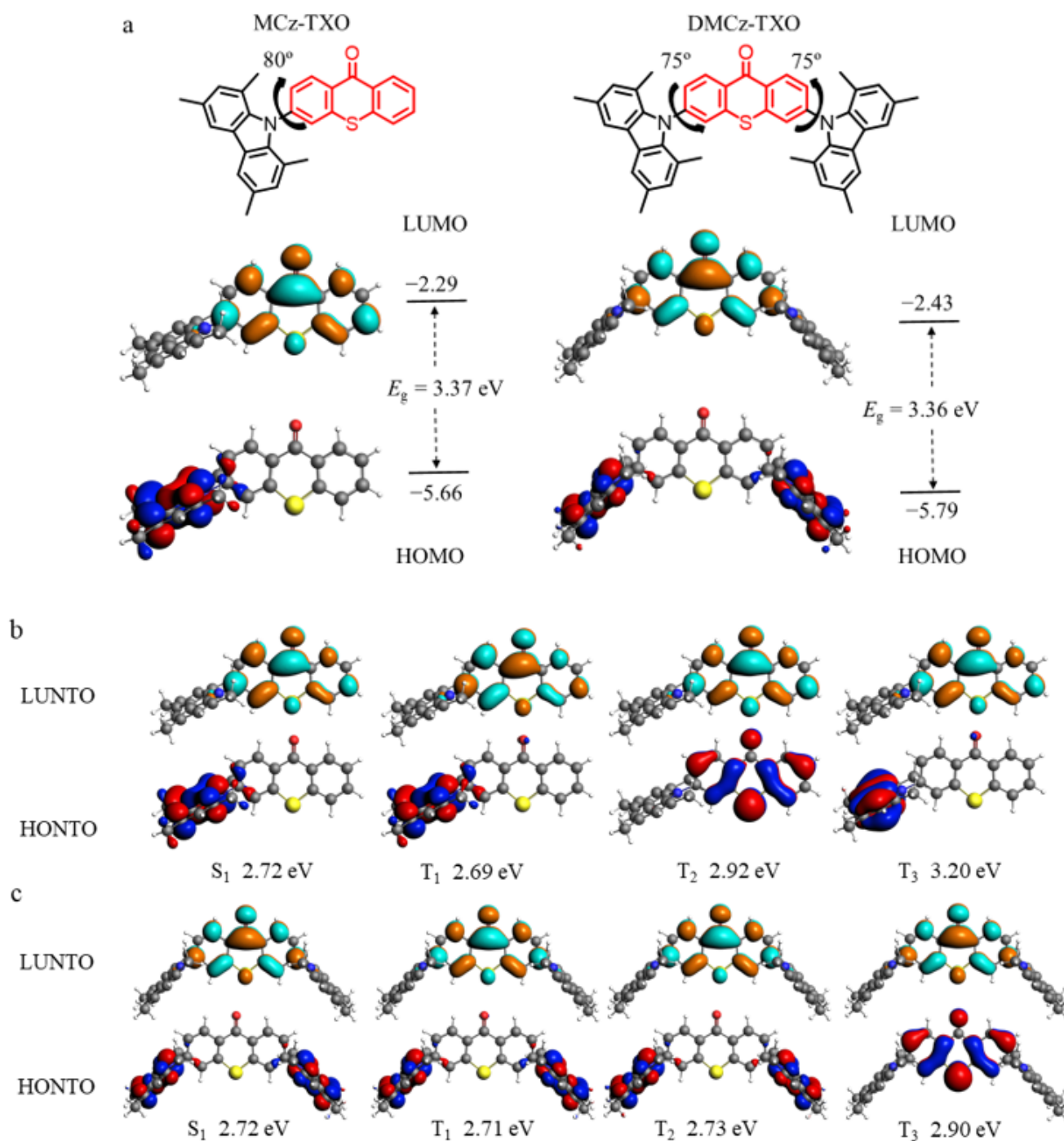


Figure 1

(a) Chemical structures and HOMO, LUMO distributions of MCz-TXO and DMCz-TXO; (b) HONTO and LUNTO distributions of excited states as well as their energy levels of MCz-TXO; (c) HONTO and LUNTO distributions of excited states as well as their energy levels of DMCz-TXO.

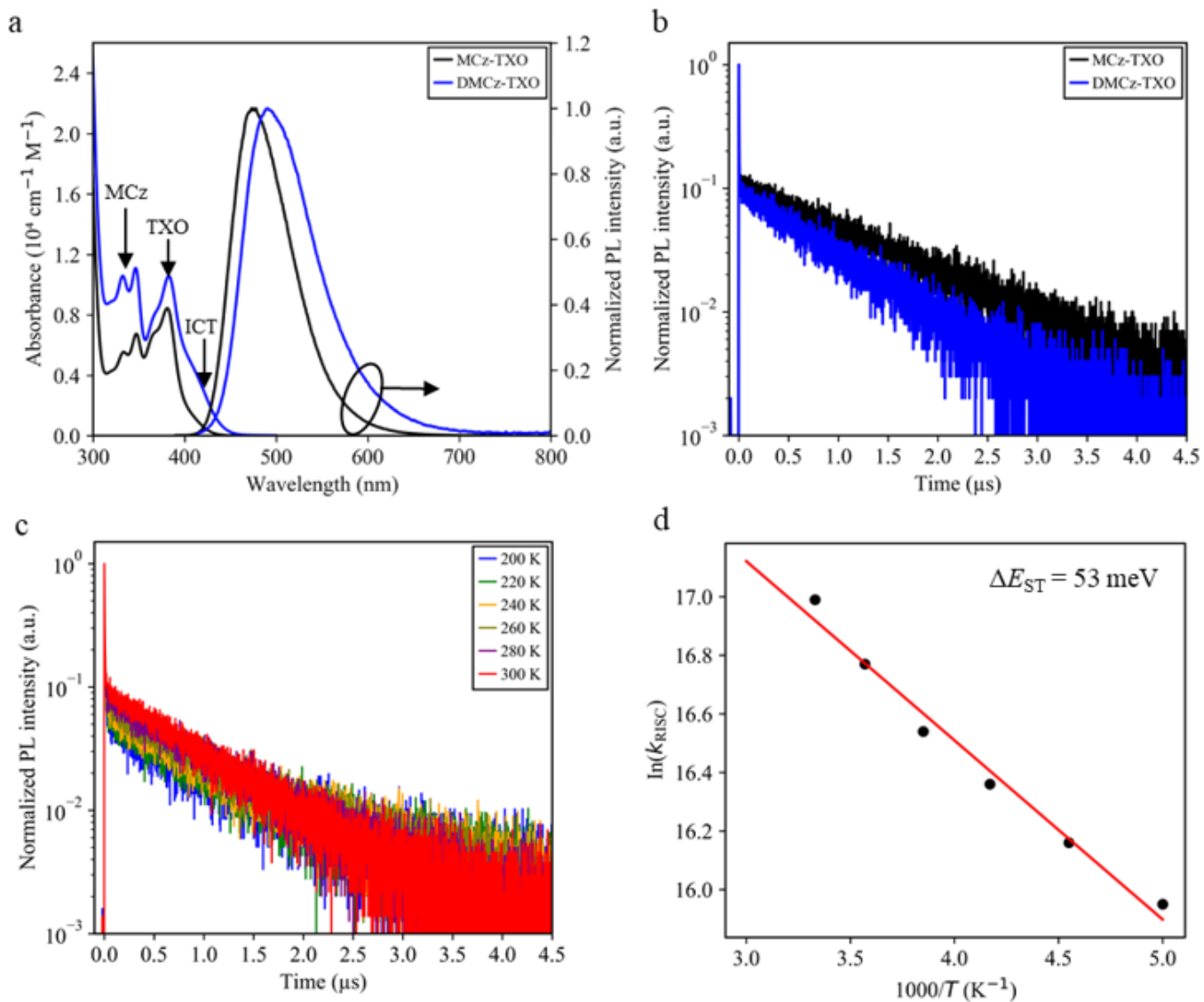


Figure 2

(a) UV-vis absorption spectra and normalized PL spectra of MCz-TXO (black line) and DMCz-TXO (blue line) in 10^{-4} M oxygen-free toluene solution at ambient temperature. (b) Transient PL decay curves of MCz-TXO (black line) and DMCz-TXO (blue line), both in 10^{-4} M oxygen-free toluene solution at ambient temperature. (c) Transient PL decay curves of 5 vol% DMCz-TXO:mCBP film from 200 to 300 K. (d) Arrhenius plot of k_{RISC} for the 5 vol% DMCz-TXO:mCBP film. The straight line is used to determine the activation energy.

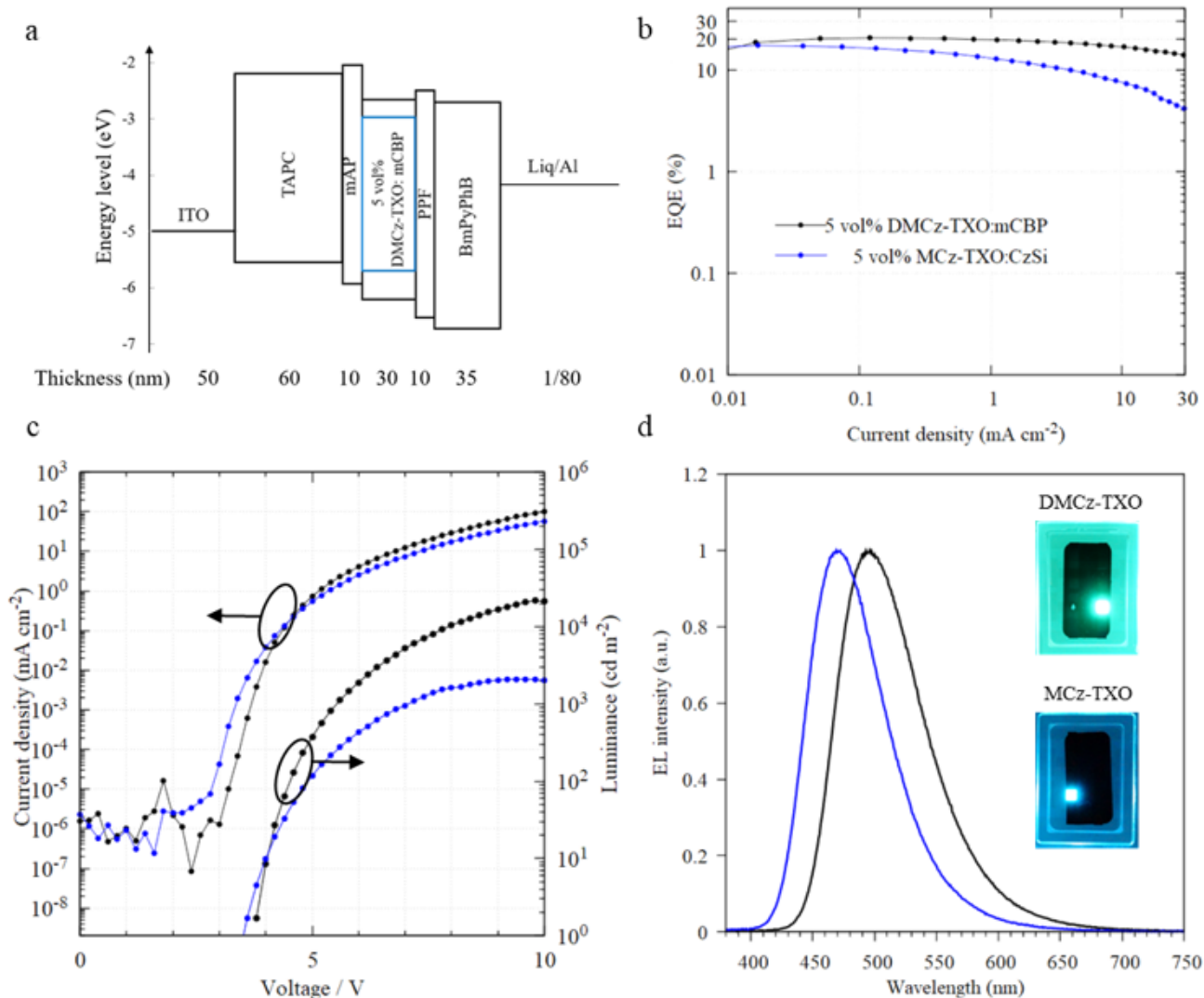


Figure 3

(a) Schematic diagrams of the 5 vol% DMCz-TXO:mCBP based device. (b) EQE versus current density characteristics of 5 vol% DMCz-TXO:mCBP based device and 5 vol% MCz-TXO:CzSi based device. (c) Current density-voltage-luminance characteristics of 5 vol% DMCz-TXO:mCBP based device and 5 vol% MCz-TXO:CzSi based device. (d) Electroluminescent (EL) spectra at 10 mA cm^{-2} of 5 vol% DMCz-TXO:mCBP based device and 5 vol% MCz-TXO:CzSi based device. The inset photographs of OLEDs showed the EL emission.

Supplementary Files

This is a list of supplementary files associated with this preprint. Click to download.

- [20210302RenSciRepSI.pdf](#)